applied sciences

MDPI

Article

Avian Collision Risk with Reference Wind Turbines: Effects of Geometry, Operation, and Flight Height Distribution

Erik Fritz *, Marco Turrini and Joep Breuer

TNO Wind Energy, Kesslerpark 1, 2288 GS Rijswijk, The Netherlands; marco.turrini@tno.nl (M.T.); joep.breuer@tno.nl (J.B.)
* Correspondence: e.fritz@tno.nl

Abstract

The expansion of wind energy, while essential for the energy transition, poses serious collision risks to birds, particularly due to the rotating blades of wind turbines. When conducting environmental impact assessments, accurate quantification of these risks is challenging, especially offshore, and it relies heavily on collision risk models. This study investigates the influence of wind turbine geometry and operational parameters on avian collision probability, utilising the Band model in combination with four well-documented reference wind turbines. By systematically varying turbine characteristics and bird flight height distributions, the analysis reveals that both turbine design and the vertical distribution of bird flight critically affect collision risk estimates. Generally, turbines with higher power ratings and larger rotor diameters exhibit lower collision probabilities, which is attributed to their lower rotor speed. The study further introduces an adaptation of the standard Band model, which incorporates a more detailed blade geometry, including local airfoil thickness and twist. With a few exceptions, this updated model increases the predicted collision probabilities. By basing the analysis on open source reference wind turbines, the present study establishes transparent methodologies and improves reproducibility and benchmarking in collision risk assessments. The results highlight the need for species- and site-specific modelling, as well as the value of refined turbine representations, to support effective mitigation strategies and nature-inclusive wind farm planning.

Keywords: collision risk modelling; reference wind turbines; flight height distribution; band-type model

1. Introduction

Wind energy is essential to achieving energy transition goals, but the rapid expansion of onshore and offshore wind farms has increased pressures on ecological systems. Therefore, offshore wind tenders increasingly require developers to assess ecological impacts. In particular, the rotating wind turbine blades pose a collision risk for resident and migratory birds. Both the reasons for collisions and possible mitigation strategies are the subject of a multitude of studies [1]. In practice, curtailment or a total turbine shutdown is often used to reduce the impact of wind turbines during peak activity periods. For example, Dutch offshore wind farms reduce rotor speeds to below two rotations per minute during peak migration nights [2]. While already challenging onshore, the data-driven quantification of offshore collision rates is hardly possible. Consequently, collision risk models (CRMs) are widely used during the environmental impact assessment of wind farms to estimate collision probabilities and expected fatalities.

Academic Editor: Wei Huang

Received: 20 June 2026
Revised: 18 July 2026
Accepted: 20 July 2026
Published: 22 July 2026

Numerous CRMs exist, whose methodology and implementation vary. Krijgsveld et al. [3] estimate the collision probability by relating the number of victims found during field searches to bird fluxes and mean traffic rates measured using radar technology. New et al. [4] developed a collision risk model, which combines avoidance rate and collision probability into a single variable homogenously distributed over a cylinder around the turbine. Kleyheeg-Hartman et al. [5] introduced an empirical flux collision model that enables the use of a species-specific collision probability, should such data be available. The model by Bretagnolle et al. [6] calculates the collisions using ”spatially explicit estimation of hazardous flight” and was applied to approximately nine million GPS tracks of bussarts collected in western France. Another prominent model was developed by Band [7], and is thus commonly referred to as Band model. This model translates bird and rotor characteristics into a collision probability. Various models have been developed around the basic principles of the Band model. Eichhorn et al. [8] calculated the collision risk of a Red Kite using an agent-based, spatially explicit model, where the collision probability of a turbine passage is calculated using the Band model equations. Humphries et al. [9] developed a stochastic wrapper around the Band model, enabling investigations into the sensitivity of the calculated collisions to the input parameters [10]. Comprehensive reviews of existing CRMs are provided by Masden and Cook [11] and Cook et al. [12].

CRMs commonly rely on bird- and turbine-related input. Bird flight characteristics, in particular, are challenging to obtain with sufficient certainty. Visual observations [13], rangefinder observations [14], or (stereoscopic) camera setups [15,16] can help to locally identify flight heights and in some cases also species-representation. GPS loggers [17,18] and radar [14,15,19–22] give a more global picture of flight paths and, to some extent, also flight height distributions. For the determination of the latter, vertical radar [23] and airplane-mounted LiDAR [24] have also been employed. Radar and LiDAR technologies bear the additional challenge of making measurements species-specific, as often desired when analysing the collision risk that wind turbines pose. Desholm and Kahlert [19] identified different migrating species based on flight speed and radar echo signature. Cook et al. [24] combined their LiDAR measurements with camera footage to validate measurements and identify species. Literature surveys on bird flight characteristics can be found in the work of Jongbloed [25] and Gyimesi et al. [26]. Additionally, Johnston et al. [27] combined data from 32 potential offshore wind farm development sites to model the flight height distributions of 25 marine bird species.

In contrast to the bird-related input parameters for collision risk models, wind turbines are theoretically well defined, yet detailed geometric and operational data are often unavailable due to intellectual property restrictions. While basic parameters such as rotor diameter and hub height are usually reported, blade geometry and wind-speed-dependent operating conditions are rarely accessible. To solve this, Schaub et al. [18] use a Generalised Additive Model to parameterise wind turbines in terms of power, maximum chord, mean rotational speed and tip speed as a function of rotor diameter while fixing the blade pitch angle. Similarly, IJntema et al. [28] used curve fits to parameterise rotational speed, blade pitch angle and maximum chord as a function of power rating. Using such fits, turbines are represented by a single rotational speed and pitch angle, and the blade geometry is scaled from a generic chord distribution based on the maximum chord value [18,28,29]. Additionally, the Band CRM reduces the blade representation to a zero-thickness sheet without accounting for the local airfoil shape and twist [7].

An alternative to these data-fitting approaches is to rely on virtual reference wind turbines (RWTs), which represent contemporary turbine designs and enable reproducible benchmarking. Widely used examples include the NREL 5 MW [30], IEA 10 MW [31,32], IEA

15 MW [33,34], and IEA 22 MW [35,36] RWTs. These turbines are extensively documented and commonly employed in aerodynamic and aeroelastic research [37–39].

The present study investigates the effect of turbine geometry and operational conditions on the collision probability calculated using the Band model equations. Basing the research on public RWTs facilitates reproducibility and benchmarking of the presented results. The collision probability is investigated as a function of wind speed and position in the rotor disc. By comparing the results for both realistic and generic flight height distributions, the significance of this input parameter is demonstrated. Furthermore, this study evaluates how a more physical blade representation, i.e., including local airfoil thickness and spanwise twist distribution, impacts the calculated collision probability.

The remainder of this paper is structured as follows. Section 2 describes the methodology, including turbine definitions, bird and wind inputs, and collision probability calculations. The results are presented in Section 3, followed by conclusions and future research directions in Section 4.

2. Methodology

In this study, collision risk probabilities are calculated using part of the Band model as implemented in stochLAB V3 [9], which requires inputs related to the wind turbine geometry and operation, to the site, and to the investigated bird species. The developed adaptation of the Band model can be incorporated in the stochLAB framework with little effort.

2.1. Reference Wind Turbines

For this study, four reference wind turbines commonly used by the wind energy community are investigated, namely, the NREL 5 MW RWT, IEA 10 MW RWT, IEA 15 MW RWT, and IEA 22 MW RWT. They are developed to enable benchmarking and comparisons between different research groups based on open source wind turbine models that are representative of the (at the date of publication) current state-of-the-art of wind turbines. Table 1 lists the key characteristics of the four reference wind turbines.

Table 1. Key characteristics of the considered reference wind turbines.

Parameter			NREL 5 MW	IEA 10 MW	IEA 15 MW	IEA 22 MW
Rated power	P_{rated}	[MW]	5	10	15	22
Rotor diameter	D	[m]	126	198	240	284
Maximum chord	c_{max}	[m]	4.65	6.02	5.76	7.22
Hub height	z_{hub}	[m]	90	119	150	170
Ground clearance height	z_{clear}	[m]	27	20	30	28
Rated wind speed	U_{rated}	[m/s]	11.4	11	10.59	11
Maximum rotor speed	Ω_{max}	[rpm]	12.1	8.68	7.56	7.061
Reference			[30]	[31,32]	[33,34]	[35,36]

Each of the RWTs is documented in terms of planform and operating conditions. The spanwise chord and twist distributions of the four reference wind turbines are shown in Figure 1a and Figure 1b, respectively.

Additionally, the chord distributions are plotted in normalised form in Figure 2. Next to the RWTs, the chord distribution of the generic 5 MW wind turbine blade used in stochLAB [9] is plotted, too. This chord distribution would be scaled based on a maximum chord value defined in the input to stochLAB to generate wind turbine blades of arbitrary size. The most prominent trend in the normalised chord distribution is that the location of maximum chord moves closer to the root with increasing power rating. In this regard, stochLAB's generic chord distribution becomes less representative towards high power rating.

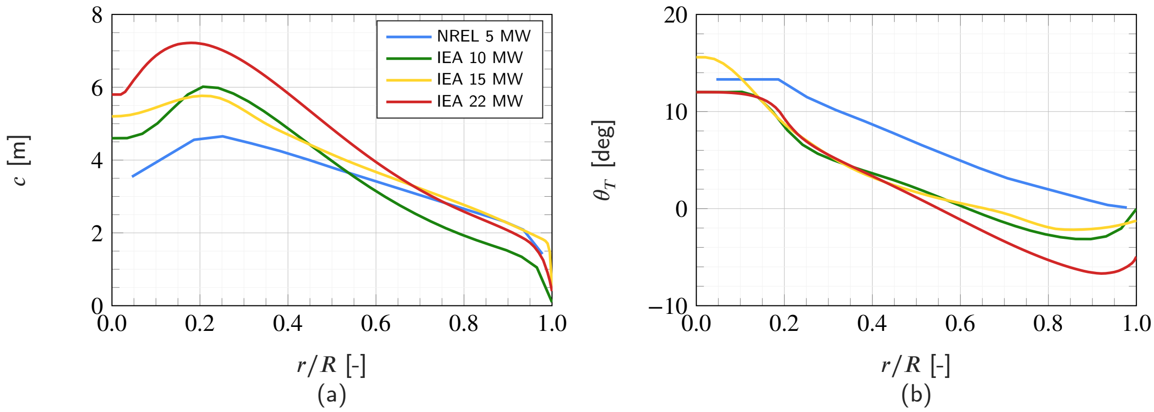

Figure 1. Chord (**a**) and twist (**b**) distribution of the reference wind turbine blades.

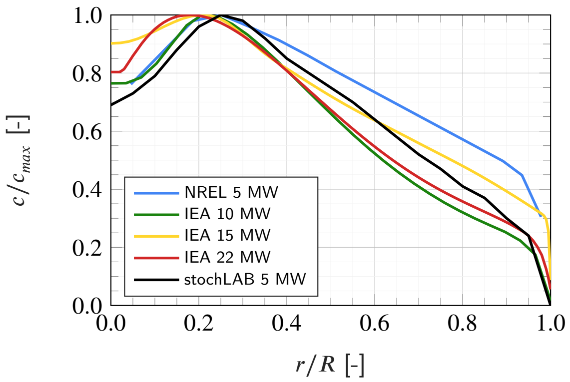

Figure 2. Normalised chord distribution of reference wind turbine blades compared to the generic turbine blade used in stochLAB.

The RWTs' operational parameters in terms of rotational speed and pitch angle are given as a function of the wind speed in Figure 3a and Figure 3b, respectively. Again, the generic input used in the stochLAB tool is given for reference. Its rotor speed curve is positioned between the NREL 5 MW RWT and the IEA 10 MW RWT. It exhibits a rather uncommon gradual increase of the rotor speed for $9\,\mathrm{m/s} \leq U \leq 16\,\mathrm{m/s}$. The pitch angle curve is aligned reasonably well with the RWTs, except for some unexpected kinks at high wind speeds. It should be noted that stochLAB offers the possibility to input the operating conditions as a function of the wind speed, as shown here, or as a probability distribution defined by the mean and standard deviation. The latter significantly reduces the fidelity to reality by neglecting the dependency on the wind speed.

The IEA 10 MW RWT's operational parameters are defined from 4 m/s onwards. For the present study, its pitch and rotor speed curves are linearly extrapolated to 3 m/s to ensure better comparability with the other RWTs.

2.2. Scenarios

The first part of this study (Section 3.1) investigates multiple scenarios in which turbine geometric parameters are varied and their impact on collision probabilities is determined. The different scenarios, schematically depicted in Figure 4, are as follows:

- Scenario A: Comparison of the different RWTs according to their definition.
- Scenario B: Comparison of the different RWTs at identical hub height. The chosen common hub height is that of the IEA 22 MW RWT, i.e., $z_{hub} = 170\,\mathrm{m}$.

- Scenario C: Comparison of the different RWTs at identical ground clearance height. Here, three sub-scenarios are considered with the clearance height varied as $z_{clear} = [25,\ 35,\ 45]$ m.

For all scenarios, both normal operation and idling conditions as occur during curtailment are investigated.

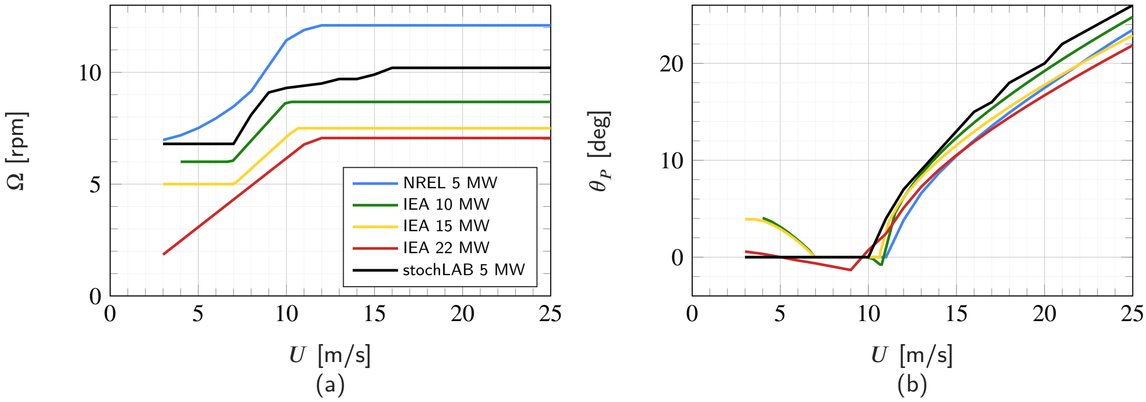

Figure 3. Rotor speed (**a**) and pitch angle (**b**) of the reference wind turbines as a function of wind speed compared to the dummy turbine parameters used in stochLAB.

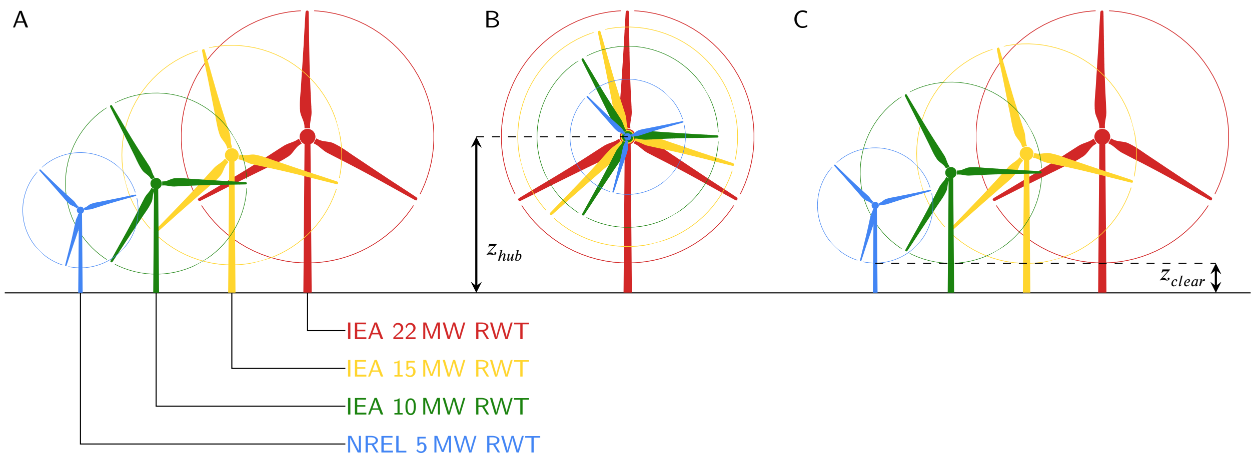

Figure 4. Scenarios for bird collision rate calculation.

2.3. Wind Input

For the presented calculations, the wind speed probability distribution p_{wind} is described by a Weibull distribution defined as

$$p_{wind}(U) = \frac{k}{\lambda}\left(\frac{U}{\lambda}\right)^{k-1} \exp\left[-\left(\frac{U}{\lambda}\right)^{k}\right], \tag{1}$$

where U is the wind speed, λ is the scale parameter, and k is the shape parameter. The scale and shape parameters are chosen as $\lambda = 10.86$ m/s and $k = 2.149$, corresponding to long-term LiDAR measurements conducted by Wouters et al. [40] at the Lichteiland Goeree platform in the North Sea. The resulting wind speed probability distribution is shown in Figure 5.

2.4. Bird Input

For the present article, the northern gannet *Morus bassanus* is chosen as a case study. This species has been the subject of multiple studies [24,28,41,42] and is well-defined in terms of physical and flight characteristics. The values for average body length, wing span, and flight speed are taken from the KEC 5.0 report [28] and are listed in Table 2.

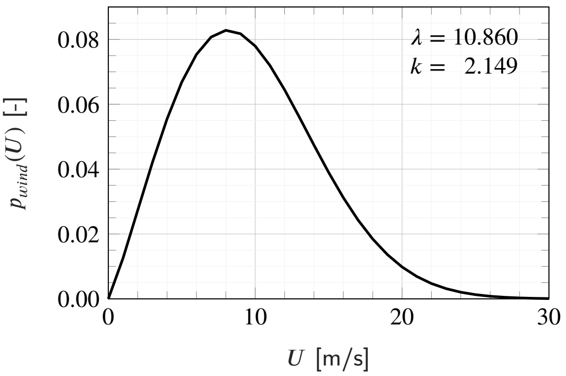

Figure 5. Wind distribution based on values reported in Wouters et al. [40].

Table 2. Physical characteristics and flight speed of the northern gannet used for the collision risk modelling taken from IJntema et al. [28].

Species			**Northern Gannet**
Body length	L_{body}	[m]	0.94
Wing span	L_{wing}	[m]	1.73
Flight speed	V_{flight}	[m/s]	13.69

The FHD of the northern gannet is taken from the data available on the stochLAB repository [9], which, in turn, is based on the paper by Johnston et al. [27]. The northern gannet has an FHD characteristic for local seabirds, with the majority of specimens flying at low altitudes. Other bird species, such as onshore raptors and migratory birds, can have significantly different FHDs. However, species-specific, tabulated data as provided by Johnston et al. [27] for seabirds are lacking in the literature. To emulate such flight behaviour, two generic FHDs are used in this study next to the realistic FHD of the northern gannet: a uniformly distributed FHD and a normally distributed FHD. The uniformly distributed FHD's value is chosen such that it sums to unity over the height for which the northern gannet's realistic FHD given in Humphries et al. [9] is defined. Such an FHD could be representative of raptors like the short-toed eagle as data presented by Schaub et al. [18] suggest, albeit based on a limited number of samples. The normally distributed FHD is defined by a mean of $\mu = 130$ m (average of the NREL 5 MW RWT's and IEA 22 MW RWT's hub heights) and a standard deviation of $\sigma = 30$ m. It is intended to approximate species with a distinct peak in their FHD rather than monotonically increasing proportions towards zero altitude. Such data are, for example, reported by Gyimesi et al. for the great black-backed gull [26]. To isolate the effect of the FHD, the bird's characteristics are kept constant to the values shown Table 2. The three flight height distributions used in this study are shown in Figure 6.

2.5. Original Band Model

The Band model [7] and "Band-type" models are the most commonly used models in analysing avian collision risks [12]. For example, they have been applied to study the collision risk of local and migratory birds in the North Sea and around the British Isles [26,28,29,41,42]. In this study, the probability of a bird colliding with the wind turbine is calculated using the equations of the Band model's second stage, which calculates the probability of collision for a bird passing through the rotor-swept area (RSA). These equations are reproduced in the following.

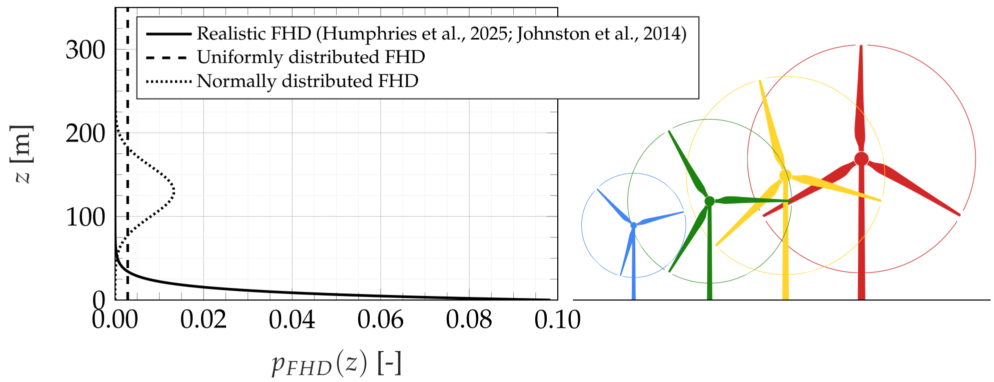

Figure 6. Flight height distribution of the northern gannet based on values reported in [9,27] and two generic flight height distributions.

The two non-dimensional parameters α and β relate the bird's flight velocity V_{flight} to the blade's local rotational velocity $\omega\, r$ and its body length L_{body} to its wing span L_{wing}, respectively:

$$\alpha = \frac{V_{flight}}{\omega\, r} \tag{2}$$

$$\beta = \frac{L_{body}}{L_{wing}}\,. \tag{3}$$

Using these parameters, the collision length L_{coll} can be calculated as

$$L_{coll} = \begin{cases} |L_{ip} + L_{op}| + L_{body} & \text{for } \alpha < \beta \\ |L_{ip} + L_{op}| + L_{wing}\, f\, \alpha & \text{for } \alpha \geq \beta \end{cases}, \tag{4}$$

where $f = 1$ for flapping flight and $f = \cos\phi$ for gliding flight. Here, ϕ is the azimuthal position in which the bird traverses the rotor disc. Northern gannets are known to alternate between flapping and gliding flight and their treatment within collision risk modelling is not standardised [43,44]. For all calculations presented in this study, flapping flight is assumed. The in-plane and out-of-plane collision length components L_{ip} and L_{op} are obtained by projecting the local chord c perpendicular and tangential to the rotor plane

$$L_{ip} = \begin{cases} +c\, \sin\theta & \text{for } \mathit{upwind\ flight} \\ -c\, \sin\theta & \text{for } \mathit{downwind\ flight} \end{cases} \tag{5}$$

$$L_{op} = \alpha\, c\, \cos\theta\,, \tag{6}$$

where c is the chord length and θ is the angle between the local airfoil's chord line and the rotor plane. In the original Band model, this angle is equated to the blade pitch angle, neglecting the local blade twist (and additional aeroelastic torsional deformations). The in-plane collision length's sign depends on whether the bird's flight is aligned with the wind direction or not, i.e., downwind or upwind flight.

The collision length obtained in Equation (4) is a function of the radial position and, thus, the collision probability is as follows too:

$$p_{coll,st}(r) = N_b\, \frac{\omega}{2\pi\, V_{flight}}\, L_{coll}(r)\,. \tag{7}$$

Here, N_b is the number of blades. The local single transit collision probability $p_{coll,st}$ is set to unity should the calculated value exceed that. The original Band model then integrates the local collision probability over the rotor disc to obtain an average single transit collision probability for a single bird transit through the rotor disc

$$\bar{p}_{coll,st} = \frac{\int_0^R p_{coll,st}(r)\, 2\pi\, r\, dr}{\int_0^R 2\pi\, r\, dr} = 2 \int_0^1 p_{coll,st}(r)\, \frac{r}{R}\, d\frac{r}{R}\,. \tag{8}$$

Next to these standard equations of the Band model, the local single transit collision probability can be related to a bird species' FHD and the local wind conditions. To this end, the single transit collision probability is calculated for each wind speed using the corresponding operating conditions ($\omega,\ \theta$) and multiplied by the probability of birds flying at the altitude corresponding to the position of the RSA. By summing over all wind speeds, a local collision probability specific to the bird and wind characteristics is obtained:

$$p_{coll}(x,y) = p_{FHD}(y) \cdot \sum_U p_{coll,st}(x,y,U) \cdot p_{wind}(U)\,. \tag{9}$$

Here, $x = r\,\sin\phi$ and $y = r\,\cos\phi + z_{hub}$ are Cartesian coordinates in the rotor disc. Equivalent to Equation (8), an average $\bar{p}_{coll}$ can be calculated based on p_{coll} by integrating over the RSA.

As discussed in Section 2.4, a single bird species is regarded in this study, represented in the Band model's second stage through the four parameters V_{flight}, L_{body}, L_{wing}, and f. If the full Band model were used, the species' turbine avoidance rate would be another important factor. Thus, the collision probability can be calculated for any species if representative values for these parameters are known.

2.6. Adjusted Band Model

Next to the original Band model, an adapted version is used in the second part of this study. This adaptation improves the fidelity with which the wind turbine blades are represented during the collision risk modelling. As discussed in the previous section, the Band model projects the chord line in the in-plane and out-of-plane directions to calculate collision length parameters. If, for example, the angle between the chord line and rotor plane is zero, the in-plane projection is zero too, while the out-of-plane projection equals the local chord. However, if one were to project the local airfoil shape rather than the chord line, the in-plane projection would be equal to the airfoil thickness, yielding a significantly different collision length. Figure 7 shows a schematic of the difference between projecting the chord line (green) or the actual airfoil geometry (light blue).

Based on this observation, the adapted Band model uses a projected airfoil geometry, expressed in its in-plane projection $L_{proj,ip}$ and out-of-plane projection $L_{proj,op}$, rather than the chord line to calculate the collision length L_{coll}:

$$L_{ip} = \begin{cases} +L_{proj,ip} & \text{for } upwind\ flight \\ -L_{proj,ip} & \text{for } downwind\ flight \end{cases} \tag{10}$$

$$L_{op} = \alpha\, L_{proj,op} \tag{11}$$

Equations (10) and (11) then substitute Equations (5) and (6) of the original Band model. Next to this change in projection, the updated Band model calculates the angle between airfoil chord and rotor plane based on the sum of the pitch angle and the local twist angle so that $\theta = \theta_P + \theta_T$. Thus, the in-plane and out-of-plane collision length components are a function of the radial position and of the airfoil families used to define the blades of the various RWTs.

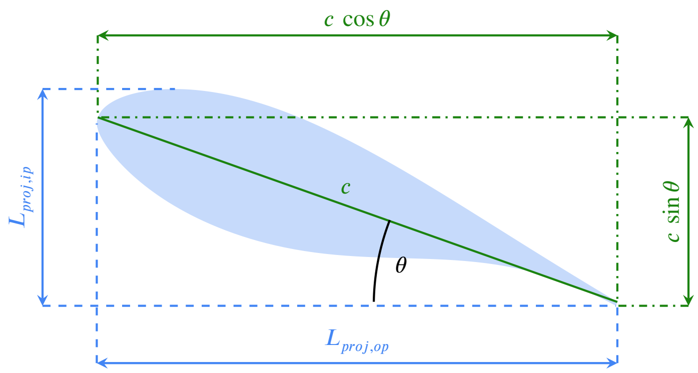

Figure 7. Schematic of the in-plane and out-of-plane projected airfoil length (light blue) compared to the projected chord length as used in the Band model (green).

3. Results

The results are presented in two stages: Section 3.1 discusses the influence of the various reference wind turbines, scenarios, and flight height distributions on the collision probability. Building on this, Section 3.2 demonstrates the impact of the updated collision length calculation methodology.

3.1. Scenario-Based Assessment of the Collision Probability

Section 2.2 defines three scenarios: Scenario A considers the RWTs as originally defined, Scenario B enforces a common hub height, and Scenario C enforces common ground clearance heights. To illustrate the underlying mechanisms, results are first discussed in detail for Scenario A, followed by a comparative assessment of all scenarios and FHDs.

Figure 8 shows the single transit collision probability distribution over the RSA of the four considered RWTs. The results are shown for $U = 8\,\mathrm{m/s}$, the most frequently occurring wind speed at the considered site (Figure 5). The most obvious trend is that the collision probability reduces with an increase in power rating. This can largely be attributed to the decreasing maximum rotor speed with increasing power rating. Additionally, there is a relatively high risk of collisions in the region of maximum chord. Towards the blade tip, where the chord tends to zero, there is a steep gradient in collision probability. Elsewhere across the RSA, collision probabilities remain approximately uniform.

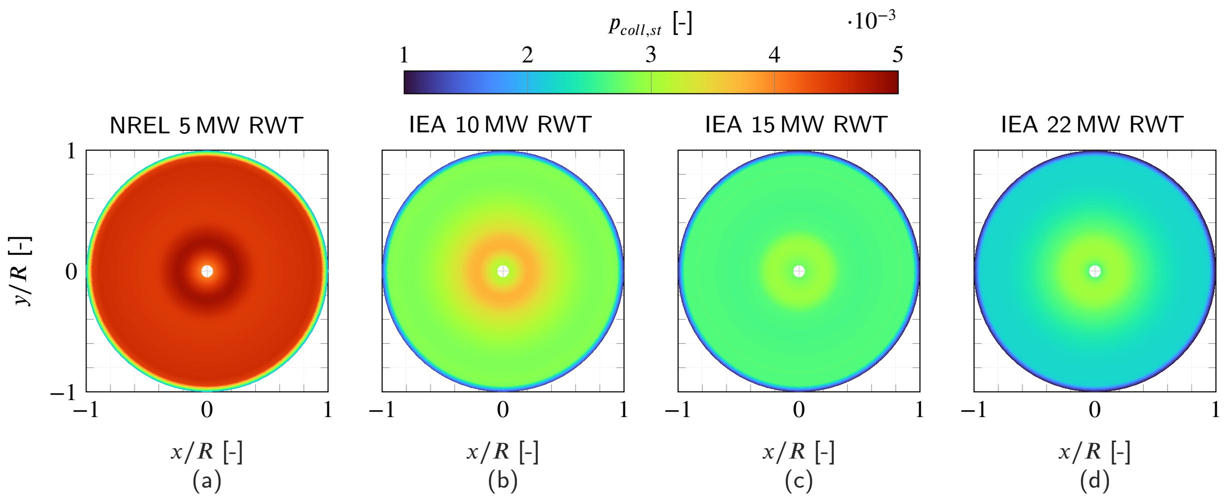

Figure 8. Single transit collision probability $p_{coll,st}$ distributed over the rotor disk of the NREL 5 MW RWT (**a**), IEA 10 MW RWT (**b**), IEA 15 MW RWT (**c**), and IEA 22 MW RWT (**d**) at a wind speed of $U = 8\,\mathrm{m/s}$.

Using Equation (8), the collision probability is integrated over the RSA, resulting in the average single-transit collision probability $\bar{p}_{coll,st}$. These values are shown in Figure 9a as a function of the wind speed assuming normal turbine operation. Throughout the investigated wind speed range, the level of collision probability is ordered inversely to the turbines' power rating. Below approximately $U = 14\,\text{m/s}$, the curves follow a trend similar to the RWTs' rotor speed curves, see Figure 3a. Beyond this wind speed, the average single-transit collision probability increases as a consequence of the pitch angle increasing, which in turn leads to a rapidly growing in-plane collision length ($L_{ip} = c\, \sin\theta$) while the out-of-plane collision length ($L_{op} = \alpha\, c\, \cos\theta$) reduces at a lower rate.

Figure 9b shows the collision probability under the assumption of an idling turbine, as could be the case during curtailment. For idling, the rotational speed is fixed at $\Omega = 2\,\text{rpm}$ [2], and the pitch angle is set to $\theta_P = 85^\circ$. As a consequence, the collision probability is independent of the wind speed. It can be seen that the idling single transit collision probability is lower than the minimum values reached during normal operation. Results are presented under the assumption that a bird has the same ability to avoid a wind turbine blade at $\Omega = 2\,\text{rpm}$ as it has at, for example, Ω_{max}. A rotor speed of $\Omega = 2\,\text{rpm}$ corresponds to blade tip speeds ranging from 13.2 m/s (NREL 5 MW RWT) to 29.7 m/s (IEA 22 MW RWT), which is a similar order of magnitude as the birds' flight speed. Therefore, this assumption is questionable from an ecological point of view. Furthermore, results are presented for the northern gannet and, thus, a seabird, while curtailment is a measure aimed at preserving migratory birds. Therefore, results should be interpreted in terms of trends for which the northern gannet serves as case study.

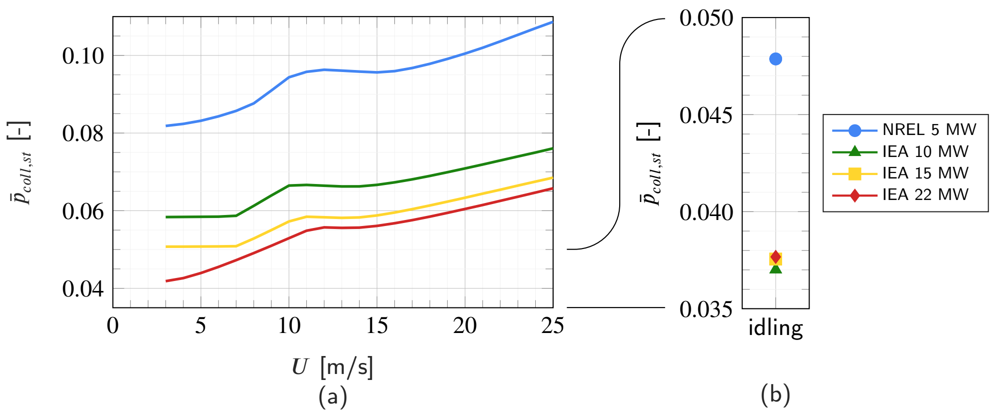

Figure 9. Average single transit collision probability $\bar{p}_{coll,st}$ as a function of the wind speed during normal operation (**a**) and idling (**b**).

To estimate the species-specific collision risk of the turbines, both the flight characteristics of the bird species and the wind speed distribution need to be taken into account. Figure 10 shows this summed collision probability (refer to Equation (9)) distributed over the RSA of the four considered RWTs. For subfigures (a–d), the realistic FHD of the northern gannet as shown in Figure 6 is used. Subfigures (e–h) show the results of an assumed uniformly distributed FHD, and subfigures (i–l) show the results using the normally distributed FHD. For all calculations, the wind distribution as shown in Figure 5 is used.

In Figure 10a–d, the realistic FHD introduces a vertical gradient into the collision probability distribution. The northern gannet mostly flies at lower heights, leading to near-zero collisions for altitudes above approximately 50 m. As a consequence, the NREL 5 MW RWT with its RSA at relatively low altitudes has a larger collision probability p_{coll} than, for example, the IEA 22 MW RWT with its RSA at higher altitudes.

Using a uniform FHD (Figure 10e–h) results in a summed collision probability directly proportional to the single transit collision probability shown in Figure 8. The resulting values are higher than those of the realistic FHD, as more birds are flying at the height of the rotor discs of the RWTs.

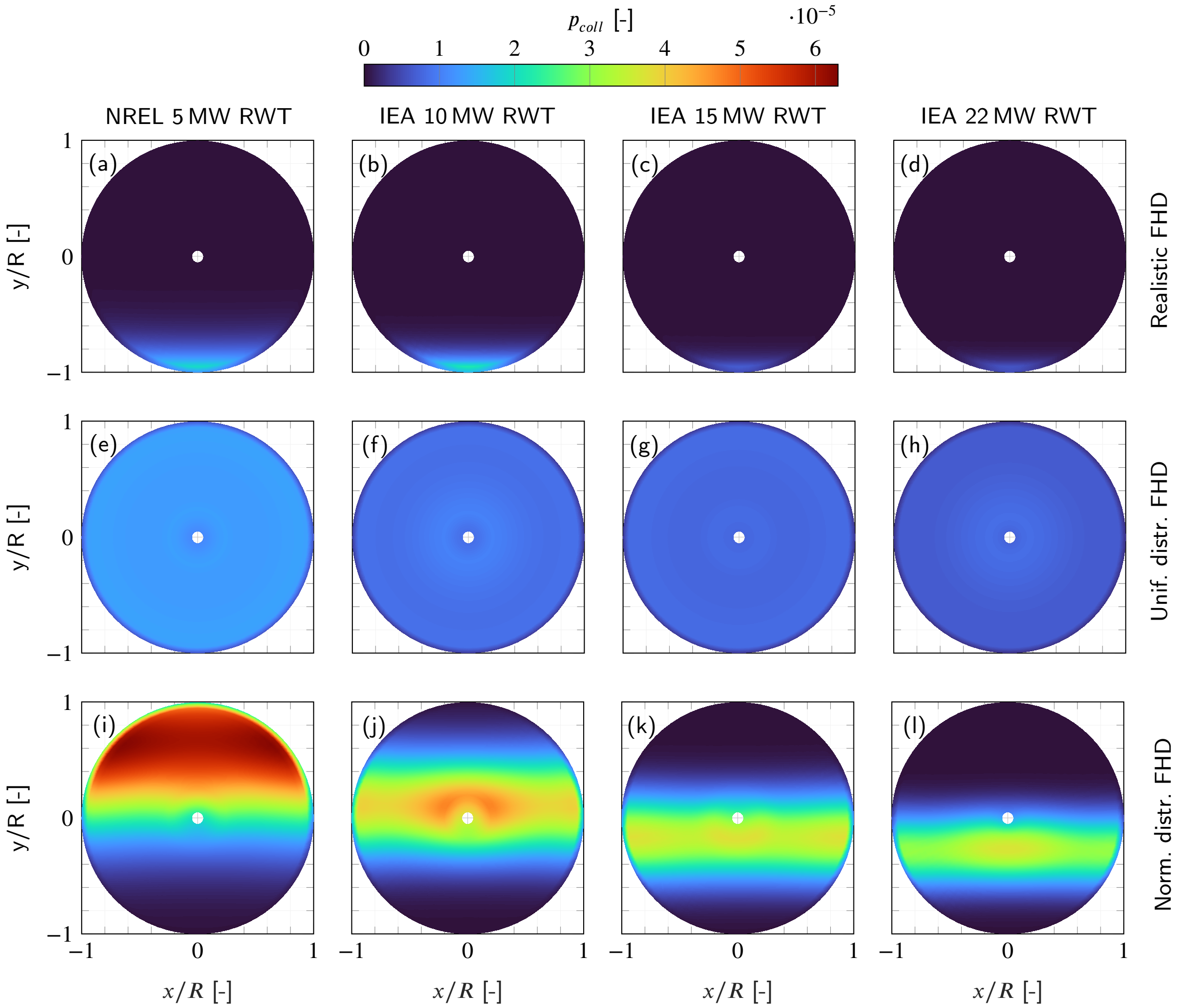

Figure 10. Summed collision probability $\bar{p}_{coll}$ distributed over the rotor disk. First column (**a**,**e**,**i**): NREL 5 MW RWT; second column (**b**,**f**,**j**): IEA 10 MW RWT; third column (**c**,**g**,**k**): IEA 15 MW RWT; fourth column (**d**,**h**,**l**): IEA 22 MW RWT. First row (**a**–**d**): realistic FHD; second row (**e**–**h**): uniformly distributed FHD; third row (**i**–**l**): normally distributed FHD.

Finally, the normally distributed FHD yields the highest summed collision probabilities for the investigated RWTs, see Figure 10i–l. For the NREL 5 MW RWT, the largest proportion of birds fly close to the highest possible point of the blade tip, yielding a much higher chance of collision in the upper half of the RSA than in the lower half. For the other RWTs, the FHD's peak is around (IEA 10 MW RWT) or just below (IEA 15 MW RWT, IEA 22 MW RWT) hub height, while barely any birds fly in the RSAs' top and bottom region. With an increase in the power rating, the level of summed collision probability reduces, which again can be attributed to the RWTs' different operating regimes.

By integrating p_{coll} over the rotor disc, the collision probability of a bird with each RWT can be expressed in a single number $\bar{p}_{coll}$. These integrated collision probabilities are shown in Figure 11 for Scenarios A–C and the realistic FHD (a), uniformly distributed FHD (b), and normally distributed FHD (c). While bar plots represent the results under normal operating conditions, markers show results during idling conditions. Note that the y-scales of the subplots differ to improve the readability of the results.

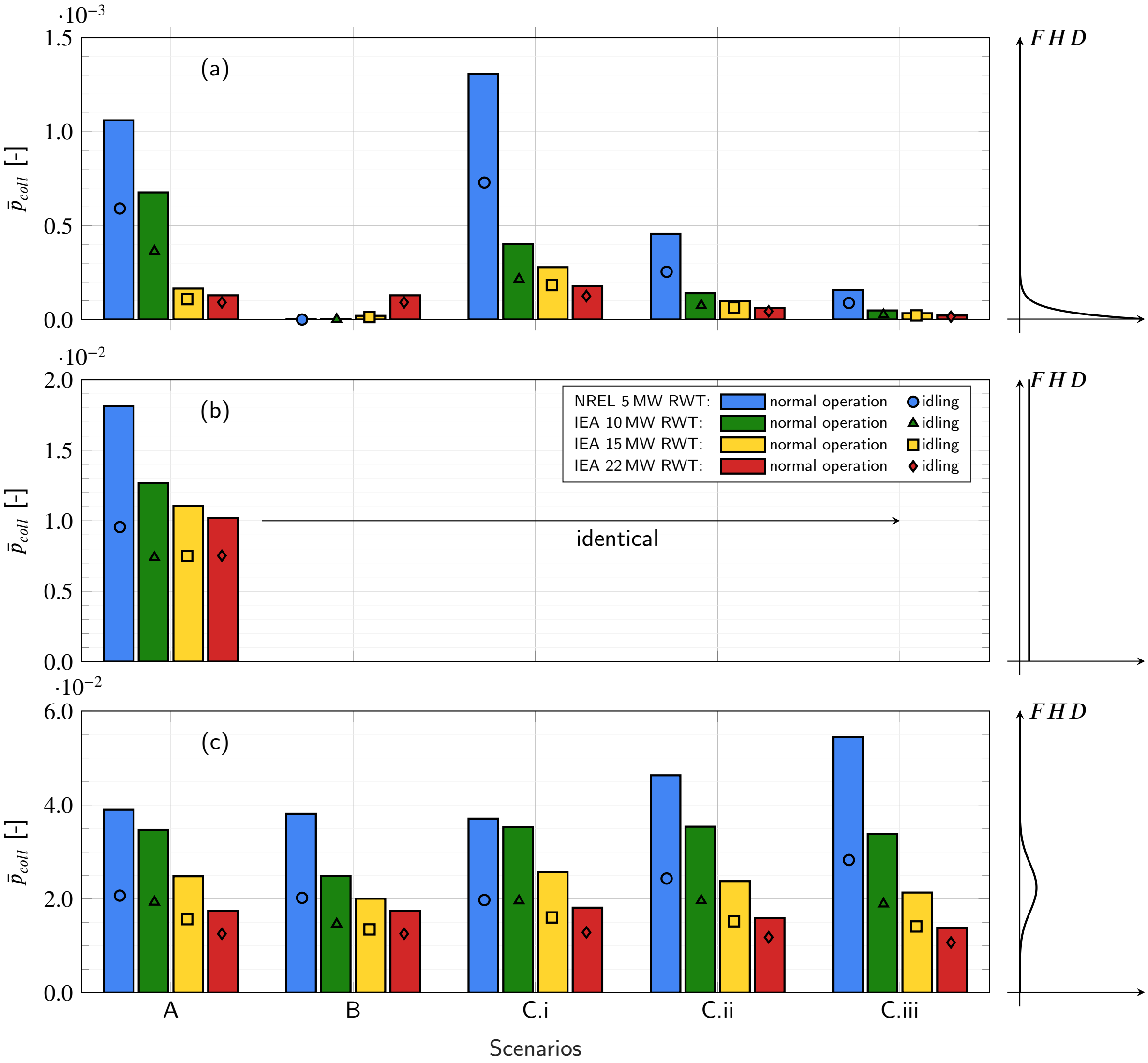

Figure 11. Average summed collision probability $\bar{p}_{coll}$ for the various scenarios under the realistic FHD (**a**), uniformly distributed FHD (**b**), and normally distributed FHD (**c**). Bars represent normal operation, while markers represent idling condition.

For the realistic FHD, variations between the different scenarios can be observed. Scenario A replicates the trend of the single transit collision probability $\bar{p}_{coll,st}$ (see Figure 9), namely, that the RWTs' collision risk is ordered inversely to their power rating. During normal operation, this trend occurs for all scenarios and FHDs with the exception of Scenario B under realistic FHD. Here, the identical hub height of $z_{hub} = 170$ m entails that only the IEA 22 MW RWT's blades pass through regions where a non-negligible proportion of northern gannets would fly. Also note that, for Scenario A and realistic FHD, the IEA 10 MW RWT exhibits a relatively high collision risk due to its definition with a relatively smaller ground clearance. Going from Scenario C.i to C.ii and C.iii, the increasing ground clearance moves the rotors away from the region where many northern gannets would fly, consequently reducing the collision probability. Idling conditions replicate the trends seen for normal operation, albeit at lower levels of collision probability. While the observed influence of the ground clearance is well-aligned with findings by Garvin et al. [45], it is worth mentioning that they found fatality rates to be positively correlated to rotor diameter and power rating, thus, contradicting this study. Such discrepancies should, however, be interpreted with care. While the present study is based on a CRM, Garvin et al. use empirical data from carcass searches. Additionally, the turbines included in the study by

Garvin et al. are relatively small ($1.0\,\text{MW} \leq P_{rated} \leq 3.6\,\text{MW}$, $61\,\text{m} \leq D \leq 136\,\text{m}$, and $55\,\text{m} \leq z_{hub} \leq 110\,\text{m}$) compared to the turbines considered here.

Figure 11b shows the summed collision probability for a uniformly distributed FHD. This FHD entails that there are no differences between the scenarios. The calculated collision probabilities are approximately one order of magnitude higher than for the realistic FHD. During idling, the three largest RWTs have a near-identical collision probability, while the NREL 5 MW RWT exhibits a slightly elevated level. Considering the equations presented in Section 2.5, the single transit collision probability $p_{coll,st}$ is a function of the chord normalised by the rotor radius during idling. The normalised chord distribution of the NREL 5 MW RWT is at a slightly higher level than that of the other three RWTs, explaining the obtained collision probabilities during idling and uniformly distributed FHD.

With a normally distributed FHD, the influence of the different scenarios becomes apparent again; however, it is not as pronounced as with the realistic FHD. The resulting collision probabilities are the highest among the three FHDs because, for most rotor configurations, the majority of birds fly at altitudes lying in the RSA. Interestingly, the ground clearance height varied in Scenario C has a different effect for the different RWTs. The NREL 5 MW RWT, with its small and low RSA, moves towards altitudes where a high proportion of birds fly if z_{clear} increases. Therefore, the collision probability increases from Scenario C.i to C.iii. For the other three considered RWTs, the trend is reversed, and an increase in ground clearance reduces the collision probability. Similar to Scenario A, the idling conditions replicate the normal operation trends at a lower collision probability.

It should be noted that the data presented in Figure 11 consider the collision probabilities of individual turbines. If one were to consider the collision risk per megawatt rated power, the trend of decreasing collision risk for turbines with higher power rating would be even more pronounced. This could be a relevant consideration when designing a wind farm with a fixed farm power rating. As an example, under realistic FHD and considering Scenario A, the NREL 5 MW RWT has a summed collision probability $\bar{p}_{coll}$ approximately 8.22 times higher than the IEA 22 MW RWT. In terms of $\bar{p}_{coll}/P_{rated}$, this factor then becomes $8.22 \cdot \frac{22}{5} = 36.17$.

3.2. Impact of Adjusting the Collision Length Calculation Methodology

In this section, the impact of the adjusted collision length calculation methodology, as described in Section 2.6, is demonstrated.

3.2.1. Difference Between Projecting the Chord Length and the Airfoil Geometry

Figure 12 shows the in-plane (a–d) and out-of-plane (e–h) projected length of the airfoil geometry for the different RWTs normalised by the local chord value. The lines per plot are coloured corresponding to the spanwise position. The blades of the various RWTs are defined using a set of airfoils located at different spanwise positions. As the RWTs are defined with different numbers of airfoils, the number of lines differs per RWT in Figure 12. The dashed lines represent the simplified chord projection used in the Band model: $c\ \sin(\theta_P)$ for the in-plane projection and $c\ \cos(\theta_P)$ for the out-of-plane projection.

The in-plane airfoil geometry projection is almost always larger than the chord line projection for identical pitch angles in the operational range. Particularly for small pitch angles, when the airfoil projection tends towards the value of the airfoil thickness while the chord line projection tends to zero, the difference becomes significant. Note that in calculating the airfoil geometry projections, the local blade twist angle has been taken into account. This is why, for some of the IEA 22 MW RWT's tip airfoils, the chord line projection (not considering local twist) can be larger than the airfoil geometry projection.

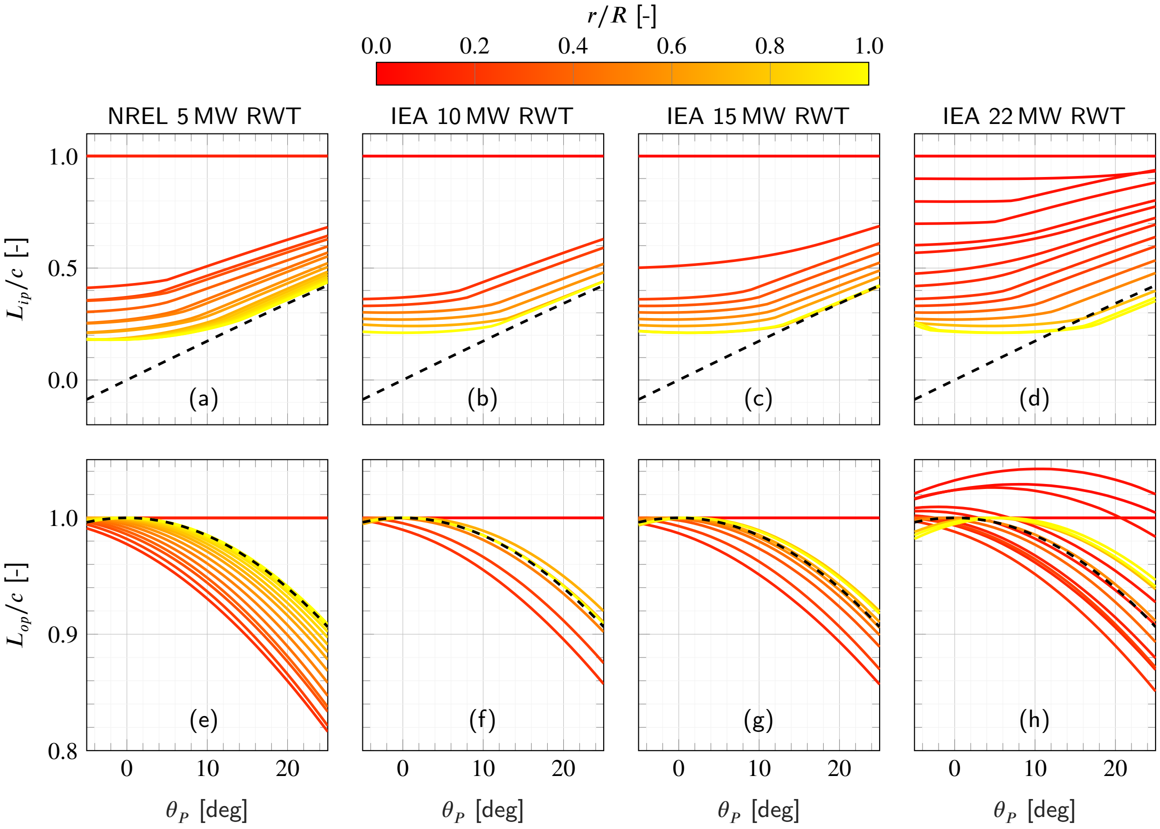

Figure 12. In-plane (**a**–**d**) and out-of-plane (**e**–**h**) projected airfoil length of the various RWTs as a function of the radial position and the blade pitch angle. Dashed lines represent the chord line projection used in the Band model.

The out-of-plane airfoil geometry projection is mostly smaller than the chord line projection. Again, this can be attributed to the omission/inclusion of the twist distribution depending on the method. The IEA 22 MW RWT has an interesting characteristic, where the airfoil geometry projection can exceed the value of its chord. This is due to the flatback airfoils used close to the root. Such airfoils have become a common choice in modern wind turbines and feature a blunt trailing edge rather than the sharp trailing edge shown in Figure 7. A rotation of the airfoil can then lead to a projected length larger than the chord value.

3.2.2. Relative Change in the Calculated Collision Probability

Analogously to the results shown in Figure 9, the single transit collision probability based on the updated collision length ($p^*_{coll,st}$) is calculated as a function of the wind speed. To relate this updated collision probability to the original values, their ratio is plotted in Figure 13a. The updated collision length calculation usually leads to higher collision probabilities, particularly for higher wind speeds. For lower wind speeds, a slight reduction in collision probability can be observed. The IEA 22 MW RWT is an exception to this, where the ratio between new and old collision probability is close to unity for low wind speeds. In idling, the increase in predicted collision risk is more significant, yielding close to a 20% increase for the NREL 5 MW RWT and approximately 10% for the other RWTs.

To understand the increased collision probability, Figure 14 shows the ratio of the new to the original single transit collision probability distributed over the rotor disc, here exemplarily shown for $U = 20\,\text{m/s}$. The increased collision probability primarily stems from the midboard region, with the highest ratios being reached at approximately $r/R = 0.4$. Here, the ratio of airfoil thickness to chord is relatively high (approximately 30%), leading to an increased projection length, particularly in the in-plane direction. Towards the blade tip, where the airfoils are thinner, and at the blade root, where the out-of-plane component dominates, the ratio of new and old collision calculations is closer to unity.

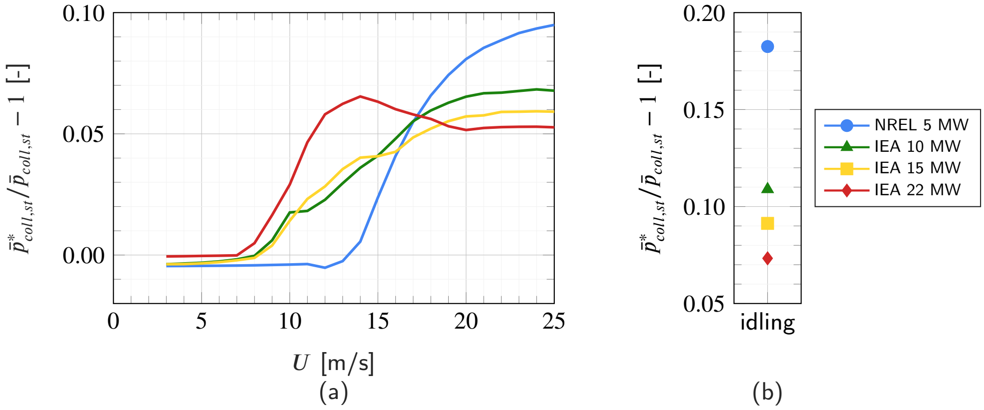

Figure 13. Ratio of the average single transit collision probability using the new and original collision length calculation as a function of the wind speed during normal operation (**a**) and idling (**b**).

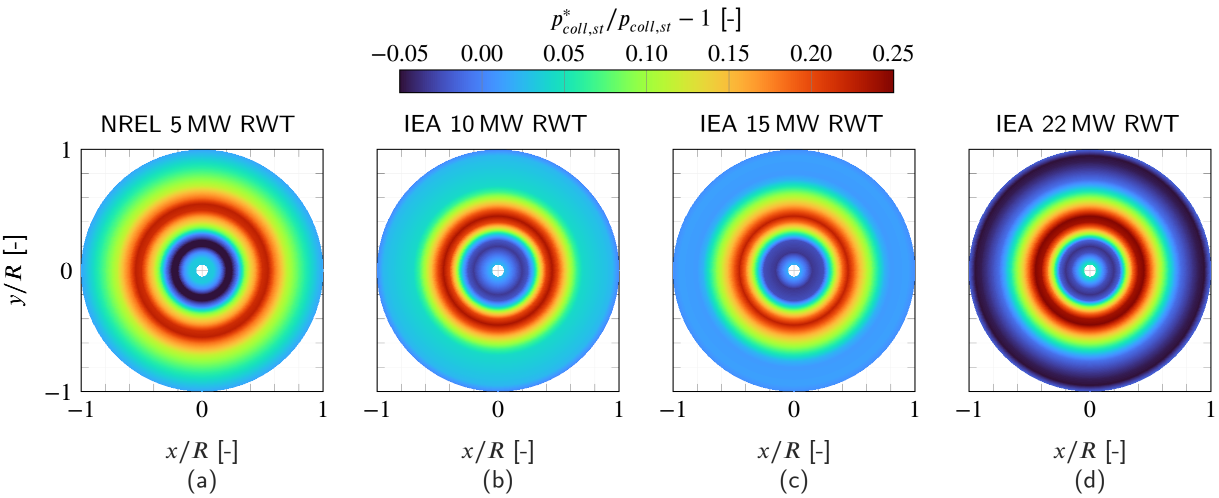

Figure 14. Ratio of the single-transit collision probability calculated using the new and old collision length implementation distributed over the rotor disk of the NREL 5 MW RWT (**a**), IEA 10 MW RWT (**b**), IEA 15 MW RWT (**c**), and IEA 22 MW RWT (**d**) at a wind speed of $U = 20\,\mathrm{m/s}$.

Using the same approach as in Section 3.1, the average summed collision probability $\bar{p}^*_{coll}$ with new collision length is calculated. Figure 15 shows the relative change between the old and new collision length methodology ($\bar{p}^*_{coll}/\bar{p}_{coll} - 1$) across the different scenarios and FHDs. For the realistic FHD, differences between scenarios are marginal for both normal operation and idling conditions because birds are only present in the lowest part of the RSA, see Figure 10a. The low relative thickness of the blade in this region yields only minor differences in the projected collision length. Between the two methodologies, the calculated collision risk increases by approximately 1–2%. The relative increase is larger for the turbines with higher power rating, which can be attributed to the lower original collision probability $\bar{p}_{coll}$ in the denominator, confer Figure 11. In idling, the IEA 15 MW RWT and IEA 22 MW RWT exhibit a decrease in collision risk. As demonstrated in Section 3.2.1, the inclusion of the twist angle in the updated collision length calculation method can lead to a lower in-plane projection towards the tip compared to the chord line projection of the original implementation. Since for the realistic FHD, birds are only present in the tip region, it is possible to obtain a reduction in calculated collision risk with the updated methodology.

For the uniform and normal FHDs, and for normal operation, the trend is similar to that of the realistic FHD, namely, that the smallest increase is observed for the NREL

5 MW RWT while the highest increase is observed for the IEA 22 MW RWT. The relative change in collision risk for the IEA 10 MW RWT and IEA 15 MW RWT is almost identical. Generally, the observed increase varies between 1% and 3%. In idling, the impact of the updated collision length calculation methodology is considerable, yielding relative increases between 4% and 22% depending on the RWT and scenario.

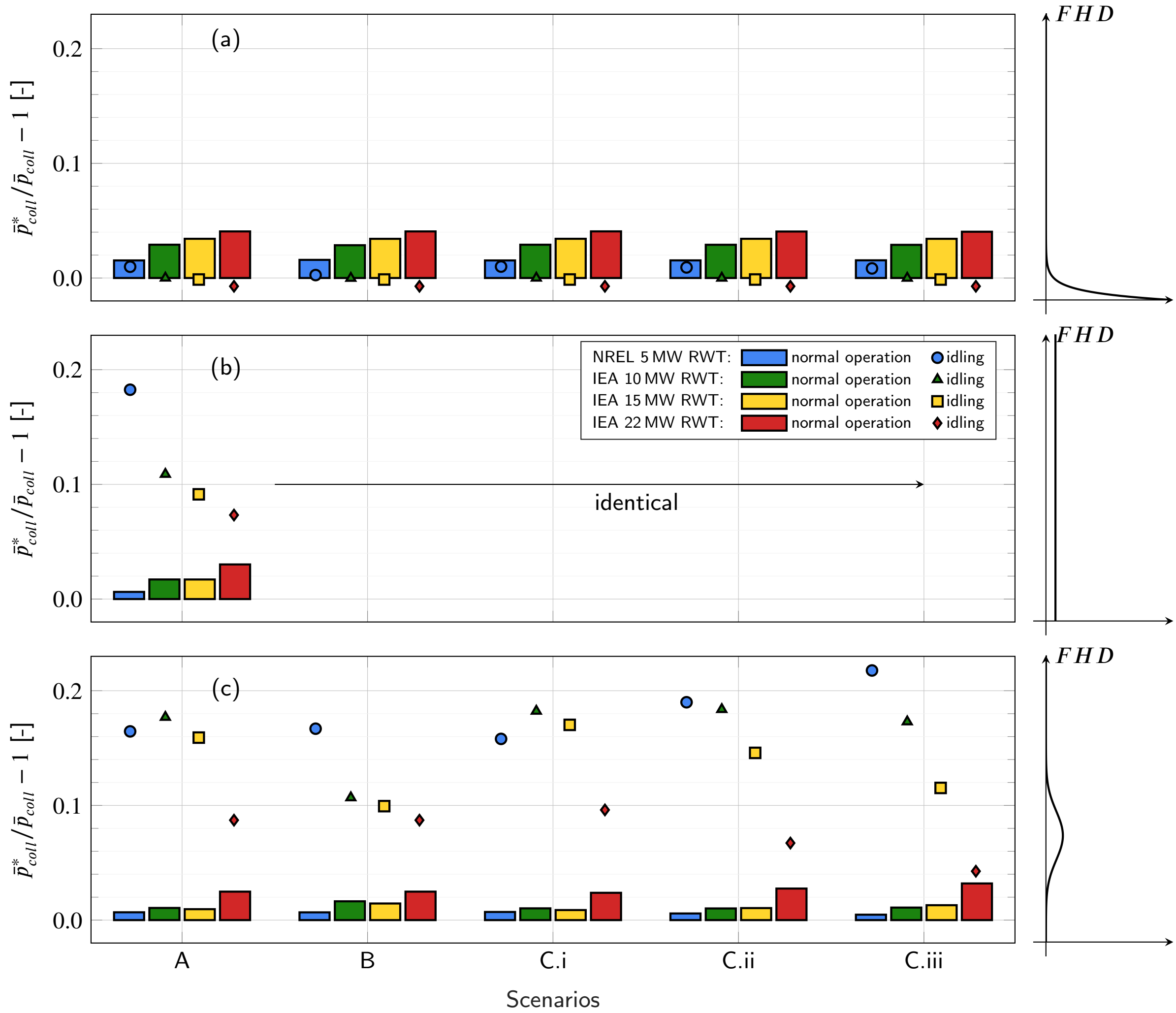

Figure 15. Relative change in the average summed collision probability due to the new collision length calculation, shown for the various scenarios under the realistic FHD (**a**), uniformly distributed FHD (**b**), and normally distributed FHD (**c**). Bars represent normal operation, while markers represent idling condition.

4. Discussion and Conclusions

This study examines how wind turbine geometry and operational conditions influence avian collision risk using the Band model and its adaptation in combination with well-documented reference wind turbines. Employing open source RWTs ensures reproducibility and benchmarking, while facilitating integration with other wind energy disciplines such as aerodynamics.

To correctly interpret the presented results, it is essential to understand the limitations of the methodology. A major challenge working with any CRM is the limited availability of validation data and benchmarking [12]. Neither quantifying the number of birds passing through a rotor disk nor quantifying collisions are easily carried out experimentally, let alone on a species level and particularly offshore. Recent measurement campaigns [15,16,46] present steps towards such quantification and encourage future research in this direction. Especially in the absence of validation data, benchmarking among various CRMs would help determining their consistency. The present study is limited to investigating the sensitivity of the Band model framework to turbine geometry and operation, flight height distribution, and model formulation. In this context, benchmarking against other CRMs is considered beyond scope.

Another limitation of this study lies in its deterministic nature. The stochLAB framework [9] allows us to define input parameters such as body length, wing span, and flight speed as probability distributions to account for variation and uncertainty. To isolate differences between the turbine scenarios and flight height distributions, the input parameters used in this study are defined as discrete values. Nonetheless, the proposed methodology—also with the adapted Band model—can be reproduced in stochLAB with distributed input parameters.

Furthermore, this study limits itself to a single bird species and a single site (represented through the wind speed distribution). When conducting an environmental impact assessment for a current or future wind farm, local species distributions and wind climate should be taken into account to reduce uncertainty in the predicted collision probabilities and to obtain indications for favourable wind turbine geometrical features such as hub height and blade tip clearance height.

Acknowledging these limitations, several conclusions can be drawn. The results show that collision probability is jointly controlled by turbine characteristics and bird flight height distributions. Turbines with higher power ratings and larger rotor diameters generally exhibit lower collision probabilities per turbine due to their lower rotor speeds. However, collision risk strongly depends on the vertical overlap between the rotor-swept area and bird flight heights, making hub height and ground clearance critical design parameters, particularly for seabirds.

Scenario analyses demonstrate that standardising hub height or ground clearance can substantially alter collision risk profiles, highlighting the need for site- and species-specific assessments. Predicted collision probabilities are also highly sensitive to the assumed flight height distribution, with uniform and normal distributions producing higher risks due to increased overlap with the rotor-swept area.

A key methodological contribution of this work is the incorporation of local airfoil thickness and spanwise blade twist into the Band model. This refinement leads to modest but consistent increases in predicted collision probabilities during normal operation. Considerable increases are observed during idling conditions and with uniformly or normally distributed FHD. The strongest effects occur where the ratio of airfoil thickness to chord is highest, underscoring the importance of detailed blade geometry in collision risk assessments. Given the lack of validation data, it remains unclear whether the refined blade representation improves the collision prediction accuracy over the original Band model with respect to reality. Positively, the new implementation does improve fidelity to the blade geometry with marginal added complexity in inputs and simulation.

Overall, these findings emphasise that robust collision risk modelling requires accurate representation of both turbine design, operation, and bird flight behaviour. Future research should focus on further refining bird flight behaviour models and improving species-specific FHD data, as well as incorporating the effect that wind speed and turbine wakes have on, for example, the flight speed, altitude, and trajectory. As discussed above, another focus should be the validation of collision predictions with actual field measurements and benchmarking CRMs among themselves. Establishing reference bird species, analogous to reference wind turbines, could further enhance comparability across collision risk studies.

Author Contributions: Conceptualization, E.F. and J.B.; Methodology, E.F., M.T., and J.B.; Formal analysis, E.F.; Writing—original draft preparation, E.F.; Writing—review and editing, M.T. and J.B.; Project administration, M.T.; Funding acquisition, J.B. All authors have read and agreed to the published version of the manuscript.

Funding: This contribution was supported by the ECOAMARE (https://www.nwo.nl/en/projects/nwa157121002, accessed on 19 July 2026) project, funded by the Dutch Research Council (NWO) under file number NWA.1571.21.002, and with internal TNO funding.

Institutional Review Board Statement: Not applicable.

Informed Consent Statement: Not applicable.

Data Availability Statement: The raw data supporting the conclusions of this article will be made available by the authors on request.

Conflicts of Interest: The authors declare no conflicts of interest.

Nomenclature

Latin letters	
c	Chord
D	Rotor diameter
f	Flight type factor
k	Shape parameter of Weibull distribution
L	Length
N_b	Number of blades
P	Power
p	Probability
R	Blade tip radius
r	Radial coordinate
U	Free stream velocity
V_{flight}	Bird flight velocity
x, y	Cartesian coordinates in rotor disc
z	Height above ground
Greek letters	
α	Ratio of flight speed to local rotational velocity
β	Ratio of bird body length to wingspan
θ	Angle between chord line and rotor plane
θ_P	Blade pitch angle
θ_T	Blade twist angle
λ	Scale parameter of Weibull distribution
μ	Mean of the normal distribution
σ	Standard deviation of the normal distribution
ϕ	Azimuth angle
Ω	Rotational speed
ω	Angular velocity
Subscripts & Superscripts	
$body$	Body length
$clear$	Refers to clearance height between lowest blade tip position and ground/water level
$coll$	Collision
FHD	Refers to the flight height distribution
hub	Hub height
ip	In-plane
max	Maximum
op	Out-of-plane
$proj$	Projection of the local airfoil
$rated$	At rated conditions
st	Single transit
$wind$	Refers to the wind speed
$wing$	Wing span

*	Refers to the collision probability with updated collision length calculation methodology

Abbreviations

CRM	Collision risk model
FHD	Flight height distribution
RSA	Rotor-swept area
RWT	Reference wind turbine

References

1. Marques, A.T.; Batalha, H.; Rodrigues, S.; Costa, H.; Pereira, M.J.R.; Fonseca, C.; Mascarenhas, M.; Bernardino, J. Understanding Bird Collisions at Wind Farms: An Updated Review on the Causes and Possible Mitigation Strategies. *Biol. Conserv.* **2014**, *179*, 40–52. [CrossRef]
2. Noordzeeloket. Start/Stop in Kavelbesluit Windpark. Available online: https://noordzeeloket.nl/functies-gebruik/windenergie/start-stop/start-stop-kavelbesluit-windpark/ (accessed on 15 October 2025).
3. Krijgsveld, K.L.; Akershoek, K.; Schenk, F.; Dijk, F.; Dirksen, S. Collision Risk of Birds with Modern Large Wind Turbines. *Ardea* **2009**, *97*, 357–366. [CrossRef]
4. New, L.; Bjerre, E.; Millsap, B.; Otto, M.C.; Runge, M.C. A Collision Risk Model to Predict Avian Fatalities at Wind Facilities: An Example Using Golden Eagles, Aquila Chrysaetos. *PLoS ONE* **2015**, *10*, e0130978. [CrossRef] [PubMed]
5. Kleyheeg-Hartman, J.; Krijgsveld, K.; Collier, M.; Poot, M.; Boon, A.; Troost, T.; Dirksen, S. Predicting Bird Collisions with Wind Turbines: Comparison of the New Empirical Flux Collision Model with the SOSS Band Model. *Ecol. Model.* **2018**, *387*, 144–153. [CrossRef]
6. Bretagnolle, V.; Merot, A.; Martineau, A.; Dedeban, E.; Chargé, R.; Debenest, E. Wind Turbine Threats to Bustards: Spatially Explicit Risk Modelling from Empirical Data. *Biol. Conserv.* **2025**, *310*, 111391. [CrossRef]
7. Band, B. *Using a Collision Risk Model to Assess Bird Collision Risks for Offshore Windfarms*; Technical Report; Strategic Ornithological Support Services: Thetford, UK, 2012.
8. Eichhorn, M.; Johst, K.; Seppelt, R.; Drechsler, M. Model-Based Estimation of Collision Risks of Predatory Birds with Wind Turbines. *Ecol. Soc.* **2012**, *17*, 1. [CrossRef]
9. Humphries, G.; Caneco, B.; Salmon, M. *stochLAB*, V3; Marine Scotland Science: Aberdeen, UK, 2025.
10. Masden, E.A.; Cook, A.S.; McCluskie, A.; Bouten, W.; Burton, N.H.; Thaxter, C.B. When Speed Matters: The Importance of Flight Speed in an Avian Collision Risk Model. *Environ. Impact Assess. Rev.* **2021**, *90*, 106622. [CrossRef]
11. Masden, E.; Cook, A. Avian Collision Risk Models for Wind Energy Impact Assessments. *Environ. Impact Assess. Rev.* **2016**, *56*, 43–49. [CrossRef]
12. Cook, A.S.; Salkanovic, E.; Masden, E.; Lee, H.E.; Kiilerich, A.H. A Critical Appraisal of 40 Years of Avian Collision Risk Modelling: How Have We Got Here and Where Do We Go Next? *Environ. Impact Assess. Rev.* **2025**, *110*, 107717. [CrossRef]
13. May, R.; Hoel, P.L.; Langston, R.; Dahl, E.L.; Bevanger, K.; Reitan, O.; Nygård, T.; Pedersen, H.C.; Røskaft, E.; Stokke, B.G. *Collision Risk in White-Tailed Eagles Modelling Collision Risk Using Vantage Point Observations in Smøla Wind-Power Plant*; Technical Report NINA Report 639; Norwegian Institute for Nature Research: Trondheim, Norway, 2010.
14. Skov, H.; Heinänen, S. Predicting the Weather-Dependent Collision Risk for Birds at Wind Farms. In *Wind and Wildlife*; Hull, C., Bennett, E., Stark, E., Smales, I., Lau, J., Venosta, M., Eds.; Springer: Dordrecht, The Netherlands, 2015; pp. 3–21. [CrossRef]
15. Breuer, J.; Fritz, E. *ZWEMT—Zwarte Wiek Expansie van Monitoring Door Technologie*; Technical Report TNO 2026 R10561; TNO: Petten, The Netherlands, 2026.
16. Skov, H.; Tjørnløv, R.S.; Armitage, M.; Barker, M.; Jørgensen, J.B.; Mortensen, L.O.; Uhrenholdt, T. High-resolution Multi-sensor Technology Reveals Low Collision Risk to Seabirds in Offshore Wind Farms. *J. Appl. Ecol.* **2026**, *63*, e70239. [CrossRef]
17. Mikami, K.; Kazama, K.; Kazama, M.T.; Watanuki, Y. Mapping the Collision Risk between Two Gull Species and Offshore Wind Turbines: Modelling and Validation. *J. Environ. Manag.* **2022**, *316*, 115220. [CrossRef] [PubMed]
18. Schaub, T.; Klaassen, R.H.; De Zutter, C.; Albert, P.; Bedotti, O.; Bourrioux, J.L.; Buij, R.; Chadœuf, J.; Grande, C.; Illner, H.; et al. Effects of Wind Turbine Dimensions on the Collision Risk of Raptors: A Simulation Approach Based on Flight Height Distributions. *Sci. Total Environ.* **2024**, *954*, 176551. [CrossRef] [PubMed]
19. Desholm, M.; Kahlert, J. Avian Collision Risk at an Offshore Wind Farm. *Biol. Lett.* **2005**, *1*, 296–298. [CrossRef] [PubMed]
20. Hüppop, O.; Dierschke, J.; Exo, K.M.; Fredrich, E.; Hill, R. Bird Migration Studies and Potential Collision Risk with Offshore Wind Turbines. *Ibis* **2006**, *148*, 90–109. [CrossRef]
21. Bruderer, B.; Peter, D.; Korner-Nievergelt, F. Vertical Distribution of Bird Migration between the Baltic Sea and the Sahara. *J. Ornithol.* **2018**, *159*, 315–336. [CrossRef]
22. Bradarić, M.; Kranstauber, B.; Bouten, W.; Van Gasteren, H.; Baranes, J.S. Drivers of Flight Altitude during Nocturnal Bird Migration over the North Sea and Implications for Offshore Wind Energy. *Conserv. Sci. Pract.* **2024**, *6*, e13114. [CrossRef]

23. Fijn, R.C.; Krijgsveld, K.L.; Poot, M.J.M.; Dirksen, S. Bird Movements at Rotor Heights Measured Continuously with Vertical Radar at a Dutch Offshore Wind Farm. *Ibis* **2015**, *157*, 558–566. [CrossRef]
24. Cook, A.S.; Ward, R.M.; Hansen, W.S.; Larsen, L.R. Estimating Seabird Flight Height Using LiDAR. *Scott. Mar. Freshw. Sci.* **2018**, *9*, 14.
25. Jongbloed, R.H. *Flight Height of Seabirds. A Literature Study*; Technical Report C024/16; IMARES: Den Helder, The Netherlands, 2016.
26. Gyimesi, A.; Evans, T.; Linnebjerg, J.; de Jong, J.; Collier, M.; Fijn, R. *Review and Analysis of Tracking Data to Delineate Flight Characteristics and Migration Routes of Birds over the Southern North Sea*; Technical Report 1-139; Bureau Waardenburg: Culemborg, The Netherlands, 2017.
27. Johnston, A.; Cook, A.S.C.P.; Wright, L.J.; Humphreys, E.M.; Burton, N.H.K. Modelling Flight Heights of Marine Birds to More Accurately Assess Collision Risk with Offshore Wind Turbines. *J. Appl. Ecol.* **2014**, *51*, 31–41. [CrossRef]
28. IJntema, G.; Heida, N.; Leemans, J.; Gyimesi, A.; Potiek, A. *Collision Effects of North Sea Wind Turbines on Bird Species Within the "Kader Ecologie \& Cumulatie (KEC) 5.0"*; Technical Report 24-163; Waardenburg Ecology: Culemborg, The Netherlands, 2025.
29. Brabant, R.; Vanermen, N.; Stienen, E.W.M.; Degraer, S. Towards a Cumulative Collision Risk Assessment of Local and Migrating Birds in North Sea Offshore Wind Farms. *Hydrobiologia* **2015**, *756*, 63–74. [CrossRef]
30. Jonkman, J.; Butterfield, S.; Musial, W.; Scott, G. *Definition of a 5-MW Reference Wind Turbine for Offshore System Development*; Technical Report NREL/TP-500-38060, 947422; National Renewable Energy Laboratory: Golden, CO, USA, 2009. [CrossRef] [PubMed]
31. Bortolotti, P.; Canet Tarres, H.; Dykes, K.; Merz, K.; Sethuraman, L.; Verelst, D.; Zahle, F. *IEA Wind Task 37 on Systems Engineering in Wind Energy-WP2.1 Reference Wind Turbines*; Technical Report NREL/TP-73492; International Energy Agency: Paris, France, 2019.
32. Bortolotti, P.; Bergua, R.; Zahle, F.; Verelst, D.; Zalkind, D.; Chetan, M.; Rinker, J. IEAWindSystems/IEA-10.0-198-RWT, 2019. Available online: https://github.com/IEAWindSystems/IEA-10.0-198-RWT (accessed on 16 July 2025).
33. Gaertner, E.; Rinker, J.; Sethuraman, L.; Zahle, F.; Anderson, B.; Barter, G.; Abbas, N.; Meng, F.; Bortolotti, P.; Skrzypinski, W.; et al. *Definition of the IEA Wind 15-Megawatt Offshore Reference Wind Turbine*; Technical Report NREL/TP-5000-75698; National Renewable Energy Laboratory: Golden, CO, USA, 2020.
34. Gaertner, E.; Rinker, J.; Sethuraman, L.; Zahle, F.; Anderson, B.; Barter, G.; Abbas, N.; Meng, F.; Bortolotti, P.; Skrzypinski, W.; et al. *Definition of the IEA Wind 15-Megawatt Offshore Reference Wind Turbine*; GitHub Repository: San Francisco, CA, USA, 2020. Available online: https://github.com/IEAWindTask37/IEA-15-240-RWT (accessed on 16 July 2025).
35. Zahle, F.; Barlas, A.; Loenbaek, K.; Bortolotti, P.; Zalkind, D.; Wang, L.; Labuschagne, C.; Sethuraman, L.; Barter, G. *Definition of the IEA Wind 22-Megawatt Offshore Reference Wind Turbine*; Technical Report DTU Wind Report E-0243; Technical University of Denmark: Kongens Lyngby, Denmark, 2024. [CrossRef]
36. Zahle, F.; Barlas, T.; Lønbæk, K.; Bortolotti, P.; Zalkind, D.; Wang, L.; Labuschagne, C.; Sethuraman, L.; Barter, G.; Marten, D. *IEAWindTask37/IEA-22-280-RWT: V1.0.1*; GitHub Repository: San Francisco, CA, USA, 2024. Available online: https://zenodo.org/records/10944127 (accessed on 16 July 2025).
37. Passon, P.; Kühn, M.; Butterfield, S.; Jonkman, J.; Camp, T.; Larsen, T.J. OC3—Benchmark Exercise of Aero-elastic Offshore Wind Turbine Codes. *J. Phys. Conf. Ser.* **2007**, *75*, 012071. [CrossRef]
38. Schepers, J.; Boorsma, K.; Sørensen, N.; Voutsinas; Sieros, G.; Rahimi, H.; Heisselmann, H.; Jost, E.; Lutz, T.; Maeder, T.; et al. Final Results from the EU Project AVATAR: Aerodynamic Modelling of 10 MW Wind Turbines. *J. Phys. Conf. Ser.* **2018**, *1037*, 022013. [CrossRef]
39. Bergua, R.; Robertson, A.; Jonkman, J.; Branlard, E.; Fontanella, A.; Belloli, M.; Schito, P.; Zasso, A.; Persico, G.; Sanvito, A.; et al. OC6 Project Phase III: Validation of the Aerodynamic Loading on a Wind Turbine Rotor Undergoing Large Motion Caused by a Floating Support Structure. *Wind Energy Sci.* **2023**, *8*, 465–485. [CrossRef]
40. Wouters, D.; van Dooren, M.; Fritz, E.; Bot, E.; Verhoef, J.; Bergman, G.; van der Werff, P. *Offshore Wind Resources at the North Sea—Lichteiland Goeree, 2014–2024*; Technical Report TNO 2025 R11109; TNO: Petten, The Netherlands, 2025.
41. Cleasby, I.R.; Wakefield, E.D.; Bearhop, S.; Bodey, T.W.; Votier, S.C.; Hamer, K.C. Three-dimensional Tracking of a Wide-ranging Marine Predator: Flight Heights and Vulnerability to Offshore Wind Farms. *J. Appl. Ecol.* **2015**, *52*, 1474–1482. [CrossRef]
42. Collier, M.; Potiek, A.; Hin, V.; Leemans, J.; Soudijn, F.; Middelveld, R.; Gyimesi, A. *Northern Gannet Collision Risk with Wind Turbines at the Southern North Sea*; Technical Report 22-052; Bureau Waardenburg: Culemborg, The Netherlands, 2022.
43. JNCC; Natural England; Natural Resources Wales; NatureScot. *Joint Advice Note from the Statutory Nature Conservation Bodies (SNCBs) Regarding Bird Collision Risk Modelling for Offshore Wind Developments*; Technical Report; JNCC: Peterborough, UK, 2024.
44. NatureScot. *Guidance Note 7: Guidance to Support Offshore Wind Applications: Marine Ornithology—Advice for Assessing Collision Risk of Marine Birds*; NatureScot: Inverness, UK, 2025.

45. Garvin, J.C.; Simonis, J.L.; Taylor, J.L. Does Size Matter? Investigation of the Effect of Wind Turbine Size on Bird and Bat Mortality. *Biol. Conserv.* **2024**, *291*, 110474. [CrossRef]
46. WEST. *A Multi-Sensor Approach for Measuring Bird and Bat Collisions with Offshore Wind Turbines (Final Technical Report)*; Technical Report 1162–FTR202510-EE0008734; Western EcoSystems Technology, Inc.: Cheyenne, WY, USA, 2025. [CrossRef]

https://doi.org/10.3390/app16147354